NUKLEONIKA 2016;61(2):131–138
doi: 10.1515/nuka-2016-0023

ORIGINAL PAPER

DE GRUYTER
OPEN

Desorption/ablation of lithium fluoride induced by extreme ultraviolet laser radiation

Tomáš Blejchař, Václav Nevrlý, Michal Vašinek, Michal Dostál, Milada Kozubková, Jakub Dlabka, Martin Stachoň, Libor Juha, Petr Bitala, Zdeněk Zelinger, Peter Pira, Jan Wild

Abstract. The availability of reliable modeling tools and input data required for the prediction of surface removal rate from the lithium fluoride targets irradiated by the intense photon beams is essential for many practical aspects. This study is motivated by the practical implementation of soft X-ray (SXR) or extreme ultraviolet (XUV) lasers for the pulsed ablation and thin film deposition. Specifically, it is focused on quantitative description of XUV laser-induced desorption/ablation from lithium fluoride, which is a reference large band-gap dielectric material with ionic crystalline structure. Computational framework was proposed and employed here for the reconstruction of plume expansion dynamics induced by the irradiation of lithium fluoride targets. The morphology of experimentally observed desorption/ablation craters were reproduced using idealized representation (two-zone approximation) of the laser fluence profile. The calculation of desorption/ablation rate was performed using one-dimensional thermomechanic model (XUV-ABLATOR code) taking into account laser heating and surface evaporation of the lithium fluoride target occurring on a nanosecond timescale. This step was followed by the application of two-dimensional hydrodynamic solver for description of laser-produced plasma plume expansion dynamics. The calculated plume lengths determined by numerical simulations were compared with a simple adiabatic expansion (blast-wave) model.

Key words: desorption • fluid dynamics • lithium fluoride • numerical simulation • plume expansion • pulsed laser ablation

Introduction

Understanding the interactions of soft X-ray (SXR) and extreme ultraviolet (XUV) radiation with solid targets is challenging for fundamental physics of warm dense matter (WDM) state, which is relevant to laser ablation and various approach to inertial

T. Blejchař, M. Kozubková
Faculty of Mechanical Engineering,
VŠB-Technical University of Ostrava,
17. listopadu 15/2172, Ostrava-Poruba, CZ 708 33,
Czech Republic

V. Nevrlý✉, J. Dlabka, P. Bitala
Faculty of Safety Engineering,
VŠB-Technical University of Ostrava,
Lumírova 13, Ostrava-Výškovice, CZ 700 30,
Czech Republic,
Tel.: +420 597 322 872, Fax: +420 597 322 980,
E-mail: vaclav.nevrly@vsb.cz

M. Vašinek, M. Stachoň
Faculty of Electrical Engineering and Computer Science,
VŠB-Technical University of Ostrava,
17. listopadu 15/2172, Ostrava-Poruba, CZ 708 33,
Czech Republic

M. Dostál
Faculty of Safety Engineering,
VŠB-Technical University of Ostrava,
Lumírova 13, Ostrava-Výškovice, CZ 700 30,
Czech Republic
and J. Heyrovský Institute of Physical Chemistry ASCR,
Dolejškova 3, Praha 8, CZ 182 23, Czech Republic

L. Juha
Institute of Physics ASCR,
Na Slovance 2, Prague 8, CZ 182 21, Czech Republic

Z. Zelinger
J. Heyrovský Institute of Physical Chemistry ASCR,
Dolejškova 3, Praha 8, CZ 182 23, Czech Republic

P. Pira
J. Heyrovský Institute of Physical Chemistry ASCR,
Dolejškova 3, Praha 8, CZ 182 23, Czech Republic
and Faculty of Mathematics and Physics,
Charles University in Prague,
V Holešovičkách 2, Praha 8, CZ 180 00, Czech Republic

J. Wild
Faculty of Mathematics and Physics,
Charles University in Prague,
V Holešovičkách 2, Praha 8, CZ 180 00, Czech Republic

Received: 30 September 2015
Accepted: 27 November 2015

confinement fusion (ICF). Quantitative description of laser ablation phenomena is critically important for practical implementation of pulsed laser deposition (PLD) technique when utilizing radiation sources at this spectral range. The behavior of optical dielectrics upon SXR/XUV-laser irradiation is the subject of particular attention and lithium fluoride (LiF) is often studied in this context as a reference large band-gap material [1–4]. Moreover, LiF is a feasible precursor of lithium atoms and ions for the purpose of tokamak diagnostics [5]. Therefore, phenomenology of pulsed laser ablation (PLA) and adequacy of models describing laser-produced plasma (LPP) plume expansion dynamic and laser blow-off (LBO) process needs to be well known in order to increase the performance of such kind of diagnostics. Effective computational strategies and approaches with wide applicability for numerical simulation of LPP plume expansion dynamics under various experimental conditions is still desirable for many experimentalists as well as engineers in material science and fusion research.

Extensive efforts were previously done concerning the LPP plume expansion in vacuum as well as in the presence of different background gases [6, 7]. Various experimental techniques and modeling approaches were employed for obtaining qualitative as well as quantitative information on the related physical phenomena. One-dimensional (1D) and quasi-two-dimensional (2D) numerical simulations of LPP expansion dynamics enabled to gain the fundamental understanding of the experimental observations, for example concerning of plume splitting phenomenon. However, multidimensional numerical simulations of fluid dynamics can bring yet unexplored insight into such complex physical phenomena. For example, shock-wave propagation after pulsed laser irradiation of Al targets under the atmospheric pressure conditions was studied by Harilal *et al*. [8] employing unsteady solver of Navier-Stokes equations in a two-dimensional axially symmetric geometry.

To best of author's knowledge, no attempts have been made yet in order to describe spatio-temporal evolution of plasma plume induced by ablation or desorption from solid targets irradiated by the pulsed SXR/XUV laser beams. In the given context, basic concepts and phenomenology of laser ablation and desorption, as well as experimental data related to SXR/XUV ablation threshold for LiF, are summarized briefly in the next section.

SXR/XUV laser ablation and desorption of lithium fluoride

Depending on the incident laser fluence F [J/cm^2] radiation-induced damage can proceed in the regime of ablation or desorption. In Ref. [9] Haglund describes laser-induced desorption as a process resulting in the emission of ions, atoms and molecules without any substantial disturbance in the surrounding surface, while laser ablation is to be associated with large-scale disruption of surface. Mechanistic criterion is also given implicitly in Ref. [9], which defines the ablation threshold as the radiation intensity (laser fluence), which causes at least a half of monolayer of the material to be eroded form the target surface by a single laser pulse.

Following the analysis of ablation/desorption craters in molecular solids irradiated by the short pulses of XUV free-electron laser [10], it was recognized that desorption is at least one order of magnitude more efficient for soft X-rays than for UV-Vis laser light. Therefore, the above mentioned Haglund's criterion was reconsidered and phenomenological model describing nonthermal desorption/ablation was proposed in Ref. [10]. The depth of crater in desorption region is defined by this model as being linearly proportional to: (i) attenuation length (l_{att}); (ii) the ratio of incident laser fluence (F) and the laser ablation threshold fluence (F_{th}), and finally (iii) efficiency of desorption (η_{des}).

On the other hand, laser ablation is traditionally recognized as a threshold phenomenon described by the logarithmic dependence of the depth of ablation crater (d_{abl}) on the incident laser fluence (normalized by the ablation threshold). Linear proportionality of d_{abl} to l_{att} implies nanometer-scale ablation rate for optical materials strongly absorbing the photons in SXR/XUV range ($l_{\mathrm{att}} \approx 10$ nm for LiF). The threshold value of XUV laser ablation for LiF crystals was first determined by Ritucci *et al*. [4], employing capillary-discharge Ne-like Ar laser operating at $\lambda =$ 46.9 nm wavelength (26.4 eV) with the pulse duration of about 1.5 ns. Microsized cracks were identified at low-fluence (subthreshold) region, which was explained by the strong thermoelastic stress on the surface and to the brittleness of the materials. Less evident cracks and a cleaner condition of ablation were found above threshold fluence due to more efficient evaporation of material.

Important measurements reported in Refs. [2, 3] revealed very low ablation threshold (~0.01 J/cm^2) for LiF exposed to picosecond SXR laser pulses, reasoned out by the occurrence of spallative ablation [1]. The ablation threshold for LiF irradiated by UV excimer laser [11] (≈1 J/cm^2) is strongly affected by the value of l_{att}, which is much higher compared to SXR/XUV spectral region meaning that laser energy is deposited into larger volumes. Taking these findings into consideration, we could conclude that the laser ablation threshold is dependent on the photon energy, pulse length as well as optical properties of the target material (mainly l_{att} as a function of wavelength λ) (see Fig. 1).

More recent experiments on LiF ablation [12] are based on utilization of a $\lambda = 46.9$ nm capillary-discharge laser (CDL) source [13], which is a compact experimental apparatus with broad range of practical applications. This instrument based on stimulated emission of neon-like argon (Ar^{8+}) ions from a 21-cm long Al_2O_3 capillary (internal diameter $\varnothing = 3.2$ mm) filled with ≈400 mTorr of Ar will be further abbreviated in this text as XUV-CDL. The XUV-CDL delivers a pulsed beam of 26.4 eV photons with an average energy of ≈10 μJ/pulse, 1.5 ns pulse duration and 3 Hz repetition rate.

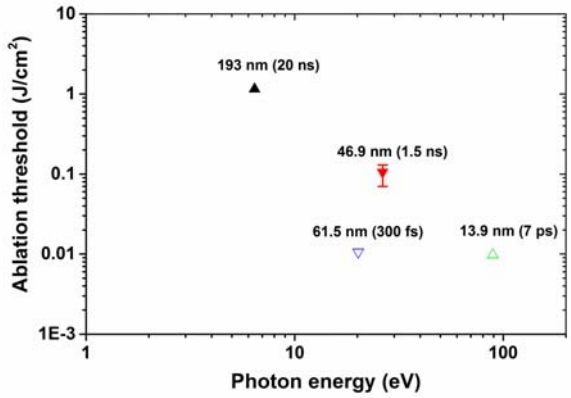

Fig. 1. Ablation threshold fluence relevant to LiF for selected lasers given here as a function of photon energy in log-log scale. Ablation threshold (symbols) for various pulsed UV/XUV/SXR laser systems with different wavelengths (specified above the symbol) and pulse lengths (given in parentheses) correspond to values reported in Refs. [2–4] (for XUV/SXR) and in Ref. [11] (for UV).

Implementation of XUV-CDL for PLA experiments performed by our group uses multilayer (Sc/Si) mirror with reflectivity $R \approx 30\%$ at the $\lambda = 46.9$ nm for focusing the laser beam onto the desired target surface. Therefore, the total energy in the focused XUV-CDL beam reaches about 3 μJ (e.g., depending on working time of Al_2O_3 capillary and other factors related to optical setup). Craters in LiF targets irradiated by the multiple pulses (multishot exposure) of focused XUV-CDL beam are characterized by presence of significant rim around the laser spot footprint of the low-fluence region, which is found at the periphery of the ablation crater. This feature was assigned to desorption regime of radiation-induced damage. The surface of LiF exposed to 10 shots of focused XUV-CDL beam, under an incidence angle of 20°, is shown in Fig. 2.

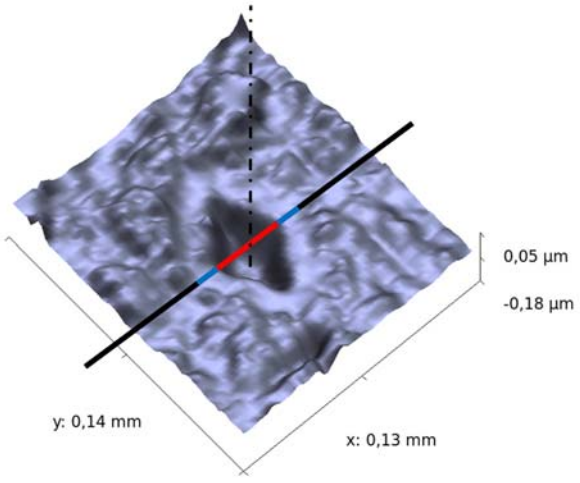

Fig. 2. Image of LiF target surface with multishot damage pattern after exposure of 10 CDL pulses in tight focus distance of target surface to mirror plane as obtained by white light interferometry (WLI) technique. The zero-level coordinate on the LiF target surface, which belongs to plane given by direction of laser beam propagation and normal to target surface, is depicted by the black line with color segments corresponding to desorption (blue) and ablation (red) region.

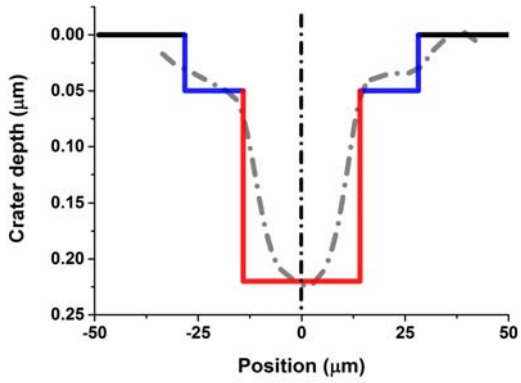

Fig. 3. The experimental crater profile (gray dash-dot line) measured along the beam propagation direction in LiF target after an exposure of 10 CDL pulses and corresponding contours of idealized desorption/ablation (blue/red) crater as predicted by XUV-ABLATOR model in two-zone approximation of laser fluence profile, that is, equivalent to relevant representative desorption and ablation rate ($d_{des} \cong 5$ nm/pulse and $d_{abl} \cong 22$ nm/pulse, respectively) multiplied by the factor of 10, accounting for 10 CDL pulses.

Samples were investigated after an irradiation (*post-mortem*) by the white light interferometry (WLI, Zygo) profiler. Desorption and ablation regimes can be distinguished also in vertical crater profile (see Fig. 3) where it is shown together with the idealized profile considering the results of prediction given by the thermodynamic model, which is described in the following section.

Modeling ns-XUV laser heating of LiF target and surface evaporation

Quantitative description of LiF desorption/ablation rate is based on modified version of thermomechanic model, which was originally written by A.T. Anderson [14]. This code (ABLATOR) was developed at Lawrence Livermore National Laboratory (LLNL) in order to predict the radiation-induced damage and feasibility of materials considered as first wall of inertial confinement fusion reactors.

Modifications of the original code were carried out previously taking into account relatively short attenuation lengths in the case of XUV ablation as well as the radiation-induced chemical decomposition occurring in ablated materials. The modified version of the code called XUV-ABLATOR, which was reported in more details elsewhere (Ref. [15]), was used for our recent study.

Briefly, XUV-ABLATOR is the Lagrangian code solving the energy balance equation along one axis (normal to the surface) employing finite difference method. It uses explicit scheme for advancing in time. Deposition of laser energy in near surface zones is governed by the Lambert-Beer law. Temperature in each zone is estimated by iterative procedure considering equations of state for condensed phase (Mie-Gruneisen) and gas phase (ideal gas law) together with enthalpy and mass conservation. The transient form of Fourier equation is used for treat-

ing the heat conduction between individual zones. Mechanical response is solved by one-dimensional finite-difference hydrodynamic model in order to predict the stress wave and material motion after the deposition of XUV-laser radiation. Material properties of lithium fluoride serving as the input data for the given study were determined based on bibliographic survey.

Computational grid size was defined by the size of the first (initial surface) zone, which was set as equal to $l_0 = 1$ nm. The total number $N = 100$ cells were included in the numerical simulations employing a XUV-ABLATOR code. The thickness l_z of the computational grid cells (z is the index ranging from 1 to $N-1$ in relevance to position of z-th zone below the initial target surface) is growing with a geometrical factor, following the formula $l_z = q \times l_{z-1}$, where $q = 1.06$ was used as a default value proposed by Anderson [14].

Attenuation length ($l_{att} = 13.6$ nm), appropriate to normal incidence angle of laser beam to LiF target, was utilized for modeling purposes. It should be pointed out that only cold opacities are considered by the recent version of XUV-ABLATOR code. Rectangular (flat-in-time) profile specifying temporal dependence of laser power within pulse duration ($\tau_p = 1.5$ ns) was assumed at the given level of approximation.

Total energy available in single pulse of the focused XUV-CDL beam $E_{tot} = 3$ μJ was assumed to be deposited on the laser spot area of $S_{tot} = 2500$ μm^2, which was divided equally into desorption and ablation region presuming the ratio of their respective area $S_{des}/S_{abl} = 3/1$. Following this criteria, the first part of laser energy $E_{des} = 1.5$ μJ was considered to irradiate the area $S_{des} = 1875$ μm^2 (yielding $F_{des} = 70$ mJ/cm^2) and the second part of laser energy $E_{abl} = 1.5$ μJ on the area $S_{abl} = 625$ μm^2 (yielding $F_{abl} = 240$ mJ/cm^2). These conditions were set as an idealized representation of observed experimental crater profiles and its typical morphology.

Temporal evolution of vertical temperature profile within the LiF target during XUV-CDL pulse is presented in Fig. 4, as obtained from the 1D numerical simulations performed by XUV-ABLATOR code under the given circumstances.

The vertical position of the interface between condensed (liquid/solid) and vaporized (gaseous) LiF decreases in time under the initial target surface (below zero-level coordinate) due to material removal process, mainly occurring in laser pulse duration period (τ_p). The resulting depth at the end of simulation ($\tau = 200$ ns) is equal to $d_{abl} = 21.5$ nm for the ablation region. This value correlates well with the ablation rate at the peak (absolute minimum) of experimental crater profile (see Fig. 3). For the desorption rate is equal to $d_{des} = 4.5$ nm, which corresponds to desorption rate observed at the periphery of experimental crater profile, in spite of relatively high surface roughness of the sample.

Further details concerning implementation of output parameters (predicted by XUV-ABLATOR) into multidimensional fluid dynamics simulation of LPP plume expansion dynamics are given below.

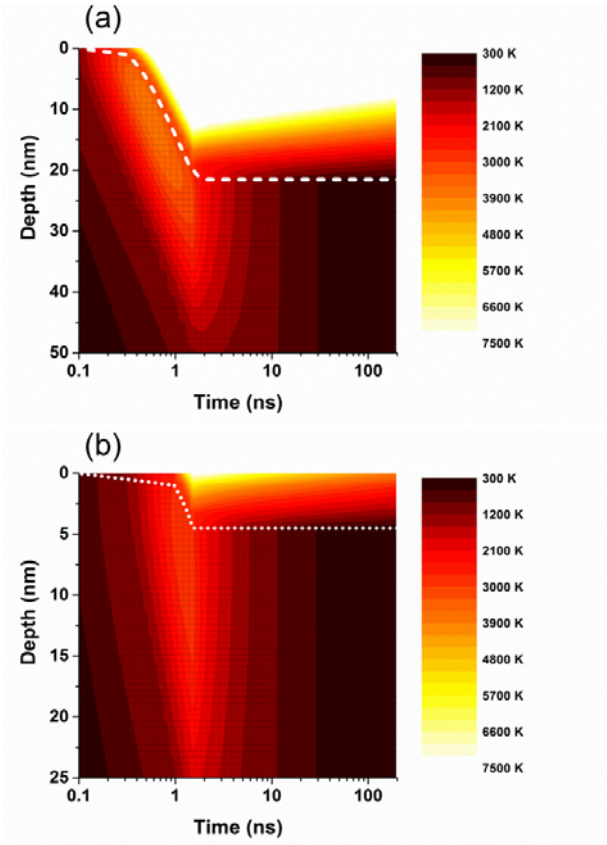

Fig. 4. Contour plots showing temporal evolution of temperature profile below the surface of the LiF target as predicted by XUV-ABLATOR code (1D thermomechanic model) for the ablation region ($F_{abl} = 240$ mJ/cm^2) depicted in (a) and desorption region ($F_{des} = 70$ mJ/cm^2) depicted in (b). Dashed white line in (a) and dotted white line in (b) describes instantaneous vertical positions of surface layer, that is, interface between condensed (liquid/solid) and vaporized (gaseous) LiF relative to initial target surface (zero-level coordinate).

Numerical modeling of LiF plume expansion

The element-based finite volume method (EbFVM) [16], as implemented in Ansys CFX software suite, was used for numerical modeling of LPP plume expansion dynamics. Whereas the problem of high-speed plume expansion is unsteady and there exists supersonic flow, then second order schemes and double precision solver has to be used. The LiF plume expansion was simulated as multispecies flow because the effect of background gas was investigated. The basic set of equations describing the unsteady compressible flow of gas mixtures can be written as follows:

$$(1) \qquad \frac{\partial \rho}{\partial t} + \frac{\partial (\rho u_j)}{\partial x_j} = 0 \quad \left[\frac{\mathrm{kg}}{\mathrm{m}^3 \cdot \mathrm{s}}\right]$$

$$(2) \quad \frac{\partial (\rho u_i)}{\partial t} + \frac{\partial (\rho u_i u_j)}{\partial x_j} = -\frac{\partial p}{\partial x_i} + \frac{\partial}{\partial x_j}\left(\eta \frac{\partial u_i}{\partial x_j}\right) \quad \left[\frac{\mathrm{kg}}{\mathrm{m}^2 \cdot \mathrm{s}^2}\right]$$

$$\frac{\partial(\rho E)}{\partial t}+\frac{\partial(\rho u_j E)}{\partial x_j}=\frac{\partial p}{\partial t}+\frac{\partial}{\partial x_j}\left(\lambda\frac{\partial T}{\partial x_j}\right)+\frac{\partial(u_j\tau_{jl})}{\partial x_l}\quad\left[\frac{\text{kg}}{\text{m}\cdot\text{s}^3}\right] \tag{3}$$

$$\frac{\partial\rho\cdot Y_{\text{LiF}}}{\partial t}+\frac{\partial(\rho\cdot u_j\cdot Y_{\text{LiF}})}{\partial x_j}=\frac{\partial}{\partial x_j}\left(\rho D\frac{\partial Y_{\text{LiF}}}{\partial x_j}\right)\quad\left[\frac{\text{kg}}{\text{m}^3\cdot\text{s}}\right] \tag{4}$$

Equation (1) represents the law of conservation (continuity equation), Eq. (2) represents the momentum equation (Navier-Stokes equation), Eq. (3) represents the law of energy conservation and Eq. (4) defines the mass fraction of component of mixture. Here ρ [kg/m³] is density, u [m/s] is velocity, t [s] is time, x [m] is the position in Cartesian coordinate system, p [Pa] is pressure, η [Pa·s] is dynamic viscosity, E [J] is the total energy, T [K] is temperature, λ [W/m·K] is thermal conductivity, τ_{jl} [Pa] is shear stress tensor, Y_{LiF} [–] is mass fraction of lithium fluoride in the plume, and D [m²/s] is diffusion coefficient.

This set of equations was closed by the perfect gas equation $(p/\rho) = R{\cdot}T/M$ where R [J/K·mol] is universal gas constant and M [g/mol] is molar mass. Since the mixture of LiF (as plume constituent) and He (as a background gas) was assumed to be present in the computational domain during the entire simulation time, the equation $(Y_{\text{LiF}} + Y_{\text{He}} = 1)$ closes the definition of gaseous mixture. The above mentioned set of equations was solved by EbFVM with coupled solver and second-order discretization scheme, which solves the hydrodynamic Eqs. (1)–(4) as a single system. This solution uses a fully implicit discretization of equations at any given time step.

Computational domain was defined in two-dimensional axisymmetric geometry with dimensions 200 μm × 500 μm consisting of 35 000 quadrilateral elements. The LPP plume expansion is expected to be initiated from the circular laser spot consisting of inner ablation region (having the radius r_{abl} = 14.1 μm) and the outer annulus with inner radius equal to r_{abl} = 14.1 μm and outer radius r_{des} = 28.2 μm). Therefore, two independent inlets are defined with nonstationary boundary conditions given as total pressure expressed from relevant pressure and temperature histories predicted by the XUV-ABLATOR code (1D thermomechanic model), as shown in Fig. 5.

A multiexponential curve fit of the temperature data was performed in order to obtain continuous temporal profiles. These algebraic expressions, that is, functions defining pressure dependence on the simulation time τ (τ = 0 corresponds to the beginning of the XUV-CDL pulse) were set as nonstationary boundary condition in two-dimensional fluid dynamics simulations. The effect of the surface regression rate and geometrical shape of the crater (~10 nm) was neglected in the given case with respect to the spatial resolution of computational grid near the inlet (~100 nm).

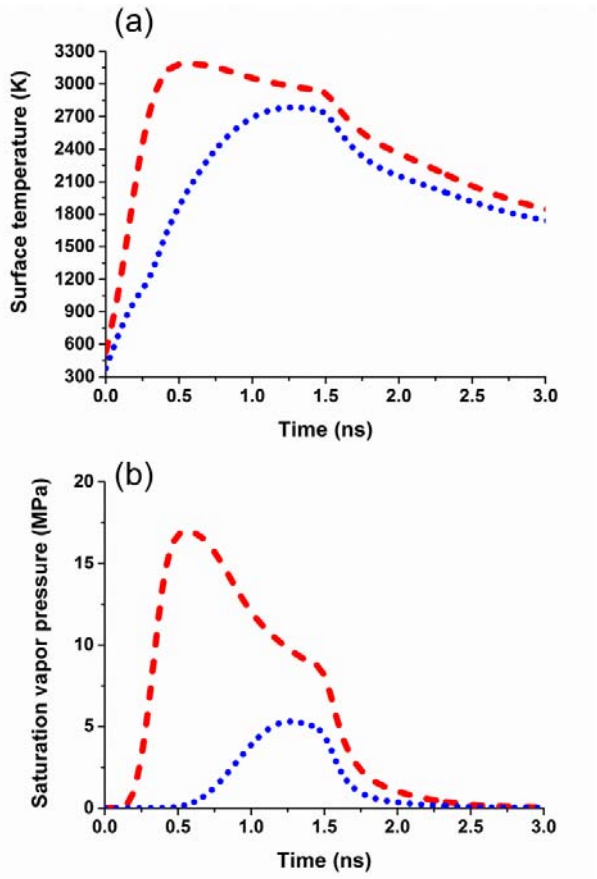

Fig. 5. Temporal evolution of surface temperature at the instantaneous interface of condensed and gas phase LiF (a) and corresponding saturation vapor pressure (b) calculated by the XUV-ABLATOR code for fluences relevant to desorption (blue dotted line) and ablation (red dashed line) region, according to Fig. 4.

The entire domain was initially assumed as being filled with He as a background gas at the moderate pressure. Two scenarios were investigated separately in frame of this study: (a) simulation of LPP plume expansion dynamics at the background pressure P_0 = 1 Torr (further referred as case A) and (b) simulation of LPP plume expansion dynamics at the background pressure P_0 = 10 Torr (further referred as case B). It is worth noting here that such moderate background pressures are not relevant to our recent PLA experiments performed under high vacuum conditions ($P_0 \approx 10^{-8}$ Torr). However, selected conditions (mostly typical for PLD experiments) were assumed in order to explore the effect of background gas pressure on XUV-LPP plume expansion dynamics and to consider further possibilities of setup adjustments.

Transient simulation of ns-XUV-LPP plume expansion dynamics was detached into three time intervals: (I) laser pulse duration and afterglow period (0–5 ns); (II) fast, that is, supersonic expansion period (5–200 ns); (III) slow, that is, subsonic, expansion (200–1000 ns). Adequate time step was assigned for these intervals on the basis of Currant number, giving 1 ps for the period (I), 5 ps for sec-

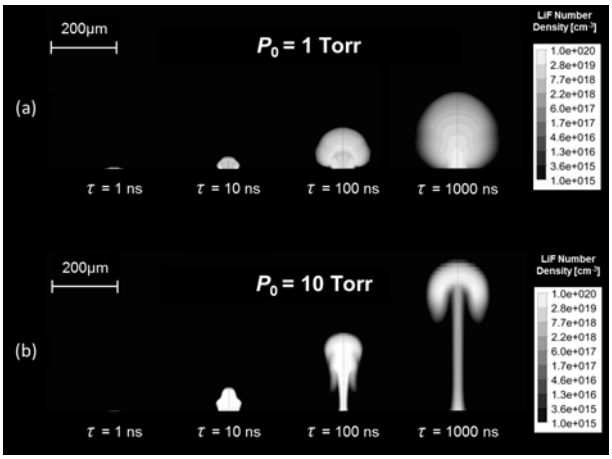

Fig. 6. Spatio-temporal evolution of ns-XUV-LPP plume at background pressures P_0 of helium relevant to the simulation of case A (a) and case B (b) described in text. Instantaneous shape of plume is characterized at selected delays times (specified below image) by the contours plot of volume number density [cm^{-3}] relevant to LiF monomer obtained from fluid dynamics simulations.

ond for the period (II), and 100 ps for the period (III). Such approach was chosen as a compromise between the size of total computational time and efficient convergence (with the criteria set as 10^{-6} for all variables) in each time step.

Results and discussion

The results of hydrodynamic simulations characterizing the spatio-temporal evolution of plume expansion dynamics are presented in Fig. 6.

A noticeable expansion (<10 μm) is observed within the period of laser pulse duration (~1 ns) in the case A as well as in the case B. After this initial period of time, visibly different plume expansion dynamics evolves for two cases studied here.

In the case A, nearly spherical plume expansion behavior can be recognized (mostly at $\tau \approx 1$ μs). The level of deceleration during the given period can be deduced from Fig. 7.

The temporal change of a plume front distance (R-τ plot) can be efficiently fitted by a viscous drag model (see e.g. Ref. [17]) in order to extract the relevant plume stopping length. On the contrary, very poor performance of drag model as well as shock model can be concluded when we aimed at fitting the R-τ plot given by the numerical simulation for the case B. Apparently, we can link this feature of R-τ plot to loss of spherical expansion behavior, which can be clearly identified in Fig. 6.

A nearly adiabatic free expansion behavior demonstrated by the quasi-spherical plume dynamics can be observed for the given condition up to about P_0 = 1 Torr He background gas pressure. At elevated background pressure (P_0 = 10 Torr), collisional effects start to dominate, leading to spatial confinement of the plasma and mushroom-like plume shape accompanying shock-wave propagation. The compression of the background gas can be considered as a shock compression process involving kinetic

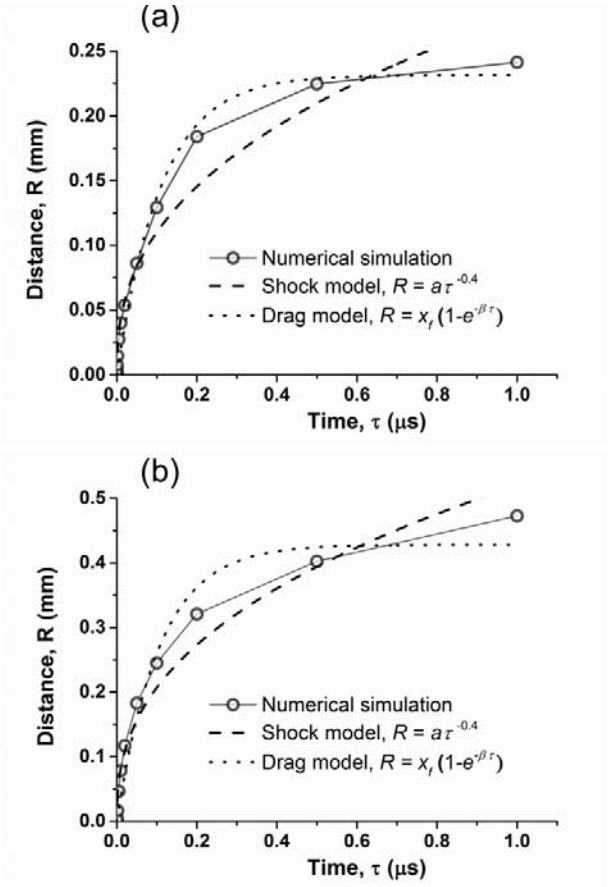

Fig. 7. R-τ plot of the expansion front boundary for the numerical simulations at the helium background pressure of P_0 = 1 Torr (a) and P_0 = 10 Torr (b). Instantaneous position of plume front was evaluated based on number density of LiF at the vertical axis of symmetry (normal to target surface) assuming the limit value of n_{LiF} = 10^{-15} cm^{-3}. Fits of these data obtained by utilizing shock model (dashed line) and viscous drag model (dotted line) are also included.

energy transfer. The shock front (high-density peaks of the background gas) propagates forward ahead of the ablated species. At the plume periphery, where the normal-to-target component of the velocity vector is vanishing, nonlinear terms corresponding to magnitude of viscous shear stress tensor are of pronounced importance.

It was observed previously [6] that as the background pressure increases from vacuum, there exists a transition regime, where the plume is characterized by a strong interpenetration of the ablated species and background gas, leading to plume splitting and sharpening. The results of our numerical simulations predicting quasi-spherical expansion at reduced pressure and the formation of mushroom-like plume shape at elevated background pressures are in qualitative agreement with these observations.

The pressure range of the transition regime depends on several factors corresponding to given experimental setup. The molar mass of ambient gas and target material vapors, laser intensity, laser spot size, and also the laser beam profile are the main parameters influencing LPP plume shape in the presence of background gas.

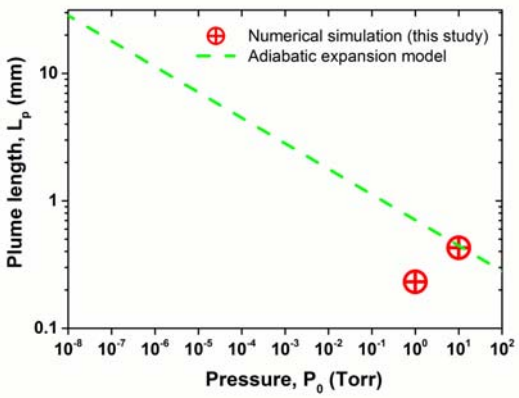

Fig. 8. Plume stopping lenght L_p estimated from adiabatic expansion (blast-wave) model (green dashed line) as a function of the background pressure in the log-log scale assuming expansion into monoatomic gas (specific heat ratio $\gamma = 1.67$) with initial velocity of $v_0 = 10^4$ m/s and expansion angle equals to 35°. For the results of numerical simulations (symbol ⊕), plume length was determined by least-square fitting of the R-τ plot to the viscous drag model, i.e., $R = L_p(1 - e^{-\beta\tau})$.

From Fig. 6 (at $\tau \approx 10$ ns), it is also obvious that difference in propagation speed of the initial volume of LiF ejected from the ablation and desorption region can play a role. Such difference is much more pronounced for case B compared to the simulation for case A. The 'faster' mass of LiF from ablation region is confined in very narrow expansion angle and with prolonged time after the initial phase ($\tau \sim 100$ ns), it can interact with the vortical structures accompanying the propagation of 'slower' component desorbed from the outer annulus of the laser spot. In order to further explore the effect of geometrical factors on the modeling output, we performed an additional numerical simulations assuming the same fluence profile as being applied at the smaller laser spot (with radii r_{des} and r_{abl} reduced by the factor of 2). In that case, more compact behavior of the shock front is observed at ($P_0 = 10$ Torr), resulting in less pronounced lateral compression of the central column compared to the case B and relatively slower expansion dynamics compared to the case A as well as compared to simulation performed at $P_0 = 1$ Torr with spot size reduction.

Based on these findings, we suggest that application of a more realistic laser beam profile is required in order to resolve the onset of the ablation near the tails of a low-fluence region, where the laser desorption occurs with considerably different dynamics of the surface evaporation. It is also evident that the results of numerical simulations at elevated background pressures leading to formation of hydrodynamic instabilities are strongly affected by the actual setup of the initial and boundary conditions. The applicability of simple mathematical models (e.g., an adiabatic expansion; i.e., a blast-wave model [18]) for the estimation of a target to substrate distance was previously proven mostly against the specific set of experimental data on LPP plume expansion dynamics. Nevertheless, several examples showing reduced predictive capabilities in relevance to PLD applications were also reported in the literature, e.g. [19]. When we compare the results of our numerical simulations with the estimated plume lengths L_p obtained from adiabatic expansion model [18] (see Fig. 8), some qualitative disagreement can be remarked. The reversed trend of plume length with increasing background gas pressure can be reasoned out by the transition to nonspherical plume expansion behavior occurring probably in the range of background pressure 1 Torr > P_0 > 10 Torr for the given laser and target parameters. Nevertheless, it should be pointed out here that quantitative evaluation of plume stopping length for the case with the loss of spherical expansion behavior would require much longer simulation time as the propagation of the confined ablated/desorbed mass is expected to continue for a prolonged period (≈10–100 μs or more). Therefore, we have to consider the perfect match with adiabatic expansion model obtained for the case B as the accidental agreement only. For a nearly spherical plume expansion observed in the case A (also obtained from the simulations with a reduced spot size) underprediction of plume length L_p by the factor of 3 have to be concluded. The effect of viscous forces considered implicitly by the solver of Navier-Stokes equations can be identified as possible source of the given discrepancy. Our recent results can thus be regarded as promising step toward realistic simulation of LPP plume expansion dynamics at the level of detail feasible for practical purposes (e.g., designing of PLD experiments) as well as for model-based interpretation of the related experiments.

Conclusions

The capability to estimate the plume stopping length based on predictive modeling at the broad range of feasible conditions is highly desirable when setting up or optimizing PLD experiment. Multidimensional numerical simulations of LPP plume expansion following ablation/desorption of XUV laser-illuminated LiF target was performed. The specific tools of continuum hydrodynamics were employed for the given purpose. It can be concluded that the system of Navier-Stokes equations can be successfully solved considering the initial and boundary conditions representative for PLD experiments ($P_0 \sim 1$ Torr of helium). We suggest that characteristic features of LPP plume expansion dynamics in different background gases can be efficiently investigated following the computational procedure described here. Finally, we would like to show the application of the ABLATOR code [14] as a demonstrative example how the models built through inertial confinement fusion related research can be used, for example, for solving some practical issues in material sciences.

Acknowledgment. This work was supported by the Czech Science Foundation (GAČR) via the project no. P108/11/1312.

This work was performed in Czech Republic at the J. Heyrovský Institute of Physical Chemistry of the Academy of Sciences of the Czech Republic, the

Institute of Physics of the Academy of Sciences of the Czech Republic, the VŠB-Technical University of Ostrava and the Charles University in Prague, Czech Republic.

References

1. Inogamov, N. A., Zhakhovsky, V. V., Faenov, A.Y., Khokhlov, V. A., Shepelev, V. V., Skobelev, I. V., Kato, J., Tanaka, M., Pikuz, T. A., Kishimoto, M., Ishino, M., Nishikino, M., Fukuda, Y., Bulanov, S. V., Kawachi, T., Petrov, Y. V., Anisimov, S. I., & Fortov, V. E. (2010). Spallative ablation of dielectrics by X-ray laser. *Appl. Phys. A-Mater. Sci. Process.*, *101*(1), 87–96. DOI: 10.1007/s00339-010-5764-3.
2. Faenov, A. Y., Inogamov, N. A., Zhakhovskii, V. V., Khokhlov, V. A., Nishihara, K., Kato, Y., Tanaka, M., Pikuz, T. A., Kishimoto, M., Ishino, M., Nishikino, M., Nakamura, T., Fukuda, Y., Bulanov, S. V., & Kawachi, T. (2009). Low-threshold ablation of dielectrics irradiated by picosecond soft x-ray laser pulses. *Appl. Phys. Lett*., *94*, 231107. DOI: 10.1063/1.3152290.
3. Inogamov, N. A., Faenov, A. Y., Zhakhovsky, V. V., Pikuz, T. A., Skobelev, I. Yu., Petrov, Yu. V., Khokhlov, V. A., Shepelev, V. V., Anisimov, S. I., Fortov, V. E., Fukuda, Y., Kando, M., Kawachi, T., Nagasono, M., Ohashi, H., Yabashi, M., Tono, K., Senda, Y., Togashi, T., & Ishikawa, T. (2011). Two-temperature warm dense matter produced by ultrashort extreme vacuum ultraviolet-free electron laser (EUV-FEL) pulse. *Contrib. Plasma Phys*., *51*(5), 419–426. DOI: 10.1002/ctpp. 201110013.
4. Ritucci, A., Tomassetti, G., Reale, A., Arrizza, L., Zuppella, P., Reale, L., Palladino, L., Flora, F., Bonfigli, F., Faenov, A., Pikuz, T., Kaiser, J., Nilsen, J., & Jankowski, A. F. (2006). Damage and ablation of large bandgap dielectrics induced by a 46.9 nm laser beam. *Opt. Lett*., *31*(1), 68–70. DOI: 10.1364/OL.31.000068.
5. George, S., Singh, R. K., Nampoori, V. P. N., & Kumar, A. (2013). Fast imaging of the laser-blow-off plume driven shock wave: Dependence on the mass and density of the ambient gas. *Phys. Lett. A*, *377*(5), 391–398. DOI: 10.1016/j.physleta.2012.11.058.
6. Harilal, S. S., Bindhu, C. V., Tillack, M. S., Najmabadi, F., & Gaeris, A. C. (2003). Internal structure and expansion dynamics of laser ablation plumes into ambient gases. *J. Appl. Phys*., *93*(5), 2380–2388. http://dx.doi.org/10.1063/1.1544070.
7. Itina, T. E., Katassonov, A. A., Marine, W., & Autric, M. (1998). Numerical study of the role of a background gas and system geometry in pulsed laser deposition. *J. Appl. Phys*., *83*(11), 6050–6054. DOI: 10.1063/1.367995.
8. Harilal, S. S., Miloshevsky, G. V., Diwakar, P. K., LaHaye, N. L., & Hassanein, A. (2012). Experimental and computational study of complex shock-wave dynamics in laser ablation plumes in argon atmosphere. *Phys. Plasmas*, *19*(8), 083504. DOI: 10.1063/1.4745867.
9. Haglund, R. F. (1996). Microscopic and mesoscopic aspects of laser-induced desorption and ablation. *Appl. Surf. Sci*., *96/98*, 1–13. DOI: 10.1016/0169-4332(95)00371-1.
10. Chalupsky, J., Juha, L., Hajkova, V., Cihelka, J., Vyšín, L., Gautier, J., Hajdu, J., Hau-Riege, S. P., Jurek, M., Krzywinski, J., London, R. A., Papalazarou, E., Pelka, J. B., Rey, G., Sebban, S., Sobierajski, R., Stojanovic, N., Tiedtke, K., Toleikis, S., Tschentscher, T., Valentin, C., Wabnitz, H., & Zeitoun, P. (2009). Non-thermal desorption/ablation of molecular solids induced by ultra-short soft x-ray pulses. *Opt. Express*, *17*(1), 208–217. DOI: 10.1364/OE.17.000208.
11. Henley, S. J., Ashfold, M. N. R., & Pearce, S. R. J. (2003). The structure and composition of lithium fluoride films grown by off-axis pulsed laser ablation. *Appl. Surf. Sci*., *217*(1/4), 68–77. DOI: 10.1016/S0169-4332(03)00583-X.
12. Pira, P., Burian, T., Vysin, L., Chalupský, J., Lančok, J., Wild, J., Střižík, M., Zelinger, Z., Rocca, J. J., & Juha, L. (2011). Ablation of ionic crystals induced by capillary-discharge XUV laser. *Proc. SPIE, 8077*, 807719. DOI: 10.1117/12.890406.
13. Heinbuch, S., Grisham, M., Martz, D., & Rocca, J. J. (2005). Demonstration of a desk-top size high repetition rate soft x-ray laser. *Opt. Express*, *13*(11), 4050–4055. DOI: 10.1364/OPEX.13.004050.
14. Anderson, A. T. (1996). *X-ray ablation measurements and modeling for ICF applications*. Doctoral dissertation, University of California, Berkeley.
15. Juha, L., Bittner, M., Chvostova, D., Letal, V., Krasa, J., Otcenasek, Z., Kozlova, M., Polan, J., Präg, A. R., Rus, B., Stupka, M., Krzywinski, J., Andrejczuk, A., Pelka, J. B., Sobierajski, R., Ryc, L., Feldhaus, J., Boody, F. P., Grisham, M. E., Vaschenko, G. O., Menoni, C. S., & Rocca, J. J. (2005). XUV-laser induced ablation of PMMA with nano-, pico-, and femtosecond pulses. *J. Electron. Spectrosc*., *144/147*, 929–932. DOI: 10.1016/j.elspec.2005.01.258.
16. Ferziger, J. H., & Peric, M. (2002). *Computational methods for fluid dynamics*. Berlin: Springer.
17. Geohegan, D. B. (1992). Physics and diagnostics of laser ablation plume propagation for high-Tc superconductor film growth. *Thin Solid Films*, *220*(1/2), 138–145. DOI: 10.1016/0040-6090(92)90562-P.
18. Dyer, P. E., Issa, A., & Key, P. H. (1990). An investigation of laser ablation and deposition of Y-Ba-Cu-O in an oxygen environment. *Appl. Surf. Sci*., *46*(1/4), 89–95. DOI: 10.1016/0169-4332(90)90125-J.
19. Zbroniec, L., Sasaki, T., & Koshizaki, N. (2002). Laser ablation of iron oxide in various ambient gases. *Appl. Surf. Sci*., *197/198*, 883–886. DOI: 10.1016/S0169-4332(02)00444-0.